Carbon 161 (2020) 423–431

Contents lists available at ScienceDirect

Carbon

journal homepage: www.elsevier.com/locate/carbon

# Evidence for a core-shell structure of hydrothermal carbon

Luke J.R. Higgins [a, **], Andy P. Brown [a], John P. Harrington [a], Andrew B. Ross [a], Burkhard Kaulich [b], Bhoopesh Mishra [a, *]

[a] School of Chemical & Process Engineering, University of Leeds, Leeds, UK
[b] Beamline I08, Diamond Light Source, Harwell Campus, Didcot, UK

ARTICLE INFO

*Article history:*
Received 4 October 2019
Received in revised form
8 December 2019
Accepted 19 January 2020
Available online 20 January 2020

ABSTRACT

Hydrothermal carbonisation (HTC) has been demonstrated to be a sustainable thermochemical process, capable of producing functionalised carbon materials for a wide range of applications. In order to better apply such materials, the local chemistry and reaction pathways governing hydrothermal carbon growth must be understood. We report the use of scanning transmission X-ray microscopy (STXM) to observe chemical changes in the functionality of carbon between the interface and bulk regions of HTC. Spatially-resolved, element-specific X-ray photo-absorption spectra show the presence of differing local carbon chemistry between bulk "core" and interface "shell" regions of a glucose-derived hydrothermal carbon spherule. STXM provides direct evidence to suggest that mechanistic pathways differ between the core and shell of the hydrothermal carbon. In the shell region, at the water-carbon interface, more aldehyde and/or carboxylic species are suspected to provide a reactive interface for bridging reactions to occur with local furan-based monomers. In contrast, condensation reactions appear to dominate in the core, removing aryl-linking units between polyfuranic domains. The application of STXM to HTC presents opportunities for a more comprehensive understanding of the spatial distribution of carbon species within hydrothermal carbon, especially at the solvent-carbon interface.



## 1. Introduction

Hydrothermal carbonisation (HTC) is a chemical process carried out in hot (180–250 °C) compressed water, whereby an organic feedstock forms a carbonaceous solid product (hydrothermal carbon), gas (CO, $CO_2$) and a chemical-rich process liquor. The first research carried out on these materials was performed during the early twentieth century, where it was found that hydrothermal carbon has similar properties to coal and may be used as fuel [1]. In the 21st century, research has returned to HTC as a green chemical route to produce sustainable carbonaceous materials with a wide range of applications including: supercapacitors, filtration devices and catalyst supports [2,4].

Renewed interest in the application of hydrothermal carbon materials has led to significant efforts being made to tune surface functionalities and physical properties (e.g. particle size, functionality) for improved effectiveness in applications. The ability to engineer hydrothermal carbon properties for specific applications requires an in-depth understanding of the physicochemical processes and formation pathways which govern HTC at molecular scale. Hydrothermal carbon formation chemistry is primarily driven by the properties of hot compressed water (HCW), which concurrently acts as a matrix, solvent, catalyst and reactant [5]. During HTC of carbohydrates, hydrothermal carbon has been shown to form *via* hydrolysis and then dehydration reactions [16–18]. Once carbohydrates have been hydrolysed, the acidic reaction conditions present in HCW catalyse dehydration reactions, probably *via* the Lobry de Bruyn-Alberta van Ekstein transformation. Dehydration reactions form the furan-based monomer: 5-hydroxymethylfurfural (HMF) [3]. HMF is suspected to be the principal monomer in the formation of hydrothermal carbon [6–8]. Glucose is known to epimerize to fructose, which subsequently forms HMF [9]. As well as HMF, furfural, levulinic acid, formic acid and acetic acid are also commonly reported to be present in the process liquor after HTC of carbohydrates; the final concentrations of HMF, furfural and organic acids depend on process temperature. Longer reaction times and higher temperatures lead to the almost complete removal of HMF from the process liquor. Therefore, it is thought that HMF reaches an equilibrium between decomposing to

* Corresponding author.
** Corresponding author.
*E-mail address:* b.mishra@leeds.ac.uk (B. Mishra).

https://doi.org/10.1016/j.carbon.2020.01.060

form organic acids, and condensing to or forming hydrothermal carbon [6,10,11]. Hydrothermal carbon formation has been hypothesised to initiate *via* the condensation of HMF to form oligomers, which grow to form hydrothermal carbon. Several condensation reactions for HMF have been proposed, including: acetone bridging, self-condensation and aldol addition - a reaction between carbonyl groups, forming a C=C double bond [12]. Once formed, hydrothermal carbon is a complex, disordered, amorphous structure of condensed furan-type subunits and typically exhibits a spherical morphology [8].

Exact pathways governing hydrothermal carbon nucleation and growth are unknown. A lack of direct observation of hydrothermal carbon nucleation chemistry is principally due to the experimental difficulty of performing *in-situ* element-specific spectroscopy during HTC. Observations have typically been carried out using kinetic modelling, assessing the size of hydrothermal carbon spherules against the concentrations of HTC liquor components [6,7,12]. The first reported formation mechanisms speculated that hydrothermal carbon spherules nucleate from oligomers and form a hydrophobic core with a hydrophilic shell *via* a La Mer type growth mechanism [10,13,14]. A more recent study by *Zhang* et al. has since provided evidence against La Mer growth, instead suggesting growth by hydrophobic ripening [15]. In the hydrophobic ripening mechanism, growth is reported to occur in three key stages: (i) the formation of HMF by the previously discussed route (ii) formation of furan-type oligomers by condensation, which eventually phase-separate from the subcritical water by formation of a hydrophobic core and hydrophilic surface, (iii) coalescence of furan-type oligomers to form hydrothermal carbon. La Mer growth predicts a shell-core structure as opposed to uniform growth by hydrophobic ripening. Direct measurement of chemical differences between the shell and core of hydrothermal carbon have proved challenging. Evidence for the original La Mer growth mechanism, was given *via* indirect observation of small differences between oxygen to carbon (O:C) atomic ratios observed using surface-biased X-ray photoelectron spectroscopy (XPS) and bulk elemental analysis (CHNS and O) [10]. The interfacial surface region of hydrothermal carbon has since been investigated by XPS, Fourier transform infrared spectroscopy (FT-IR) and transmission electron microscopy (TEM) [16–18]. These measurements have not, as yet, provided direct confirmation of differing carbon chemistry between a shell and core in hydrothermal carbon. Further, element-specific bulk spectroscopy such as $^{13}C$ NMR are not able to spatially resolve differences between the surface and bulk of hydrothermal carbon. Formation of hydrothermal carbon is a phase separation process under HCW conditions [6]. Hence, studying chemical alterations between the hydrothermal carbon interface, bulk material and surrounding aqueous environment is perhaps the most likely route to elucidate reaction pathways that underpin hydrothermal carbon formation and growth.

In this study, we have applied scanning transmission X-ray microscopy (STXM), a synchrotron-based spectromicroscopy technique, to a thin section of a glucose-derived hydrothermal carbon spherule. Using STXM, images at the tens of nanometre scale are collected as a function of transmitted X-ray energy and, in this way, the image gains chemical sensitivity *via* near-edge X-ray absorption fine structure (NEXAFS) [19,20]. There are reports of STXM being used to study a variety of carbonaceous macromolecules including: soils [21,22], humic acids [23,24], soot [25] and polymers [26]. Differences in surface and bulk carbon chemistry have also been identified in carbonaceous interfaces and thin films [27–30] and in similar, but non-hydrothermal, green carbon materials [31]. For this study, TEM imaging and STXM spectromicroscopy are applied in a synergetic analysis of a focussed ion beam milled, thin section, providing the first direct experimental evidence for a core-shell type structure in hydrothermal carbon. Further, the chemical sensitivity of STXM is used to identify changes in carbon speciation between the core and shell regions, which may indicate hydrothermal carbon formation mechanisms.

## 2. Experimental

### 2.1. Hydrothermal carbonisation of glucose

The hydrothermal carbonisation of 10 % glucose (≥99.5 %, Sigma) solution was performed in a 600 ml benchtop hydrothermal reactor (Parr, USA) at 200 °C and 250 °C under autogenic pressure as reported in previous work by our group [32]. For each run, 20 g of glucose was dissolved in 200 ml of ultra-pure (≥18 Ω) water. The prepared glucose solution, when completely dissolved, was loaded into a quartz liner and subsequently placed into the reactor. Once sealed, the reactor was heated using a resistance jacket (5 °C $min^{-1}$) to temperature, then held for 1 h before the reactor was allowed to naturally cool to room temperature. The resulting solid was recovered by filtration without a solvent wash. A solvent wash, or soxhlet extraction was not performed in order to (i) reduce the risk of introducing erroneous features into the C *K* edge X-ray spectroscopy arising from the presence of organics used for extraction and (ii) to avoid removing chemically-relevant macromolecules which were found to be removed during extraction in ethanol (Fig. S1). The recovered char was dried at 80 °C for 24 hrs and stored in sealed glass jars. Percentage yield was calculated by the quotient of the initial feedstock and the derived hydrothermal carbon on a dry basis.

### 2.2. Elemental analysis

Elemental (C, H, N and S) and oxygen analysis were performed using a FLASH-EA2000 elemental analyser fitted with an autosampler and thermal conductivity detector (Thermo Scientific). The instrument used He as a carrier gas (BOC; CP Grade), with flow rates of 140 mL $min^{-1}$ (sample side) and 100 mL $min^{-1}$ (reference side). For CHNS analysis 1.5–2.5 mg of sample were encapsulated in tin squares and analysed using a pre-packed CHNS oxidation/reduction reactor (CE Instruments Ltd) with oxygen as the oxidising gas (BOC; Grade N5.0) at a temperature of 900 °C. Oxygen analysis was performed with 2–3.5 mg of sample encapsulated in silver squares and analysed using a pre-packed pyrolysis reactor (Elemental Microanalysis Ltd) at a temperature of 1050 °C. Both CHNS and oxygen analyses were performed in triplicate with a set of relevant analytical reference materials.

### 2.3. Resin embedding, focussed ion beam (FIB) milling and SEM imaging

Samples for both forms of transmission microscopy (STXM, TEM) must be prepared so that they are ~100 nm thickness. This was achieved by setting a few milligrams of sample in Epofix resin (48 h, 25 °C), then polishing to a finish using 6 μm diamond paste. A 30 nm Iridium sputter coating was then applied to the prepared resin block using a high-resolution sputter coater (Agar, UK). Thin lamellae of sample were prepared *via* the in-situ lift-out method using a FEI Helios G4 CX Dual Beam - High resolution monochromated, field emission gun, scanning electron microscope (FEGSEM) with precise Focused Ion Beam (FIB). After transferring the coated resin block to the Dual Beam microscope, 500 nm of electron beam Platinum (Pt) was deposited (at 5 kV, 6.4 nA for the electron source) to the surface of the target area. This was followed by a second Pt layer (1 μm) using the FIB (at 30 kV, 80 pA for the liquid Ga ion source). A bulk lamella was initially cut (by the FIB at

30 kV, 47 nA), before a final cut-out was performed (at 30 kV, 79 nA). Final thinning and polishing of the lamellae to electron translucency was performed with a final polish/clean with a gentle ion beam (5 kV, 41 pA). The lamellae were attached, using Ion Beam Pt, to a copper FIB lift-out grid (Omniprobe, USA) mounted within the SEM chamber (in-situ) and then stored under vacuum before and during transport to and from the TEM and synchrotron radiation source.

### 2.4. X-ray photoelectron spectroscopy, powder X-ray diffraction and laser diffractometry

XPS was carried out with an Enviro-ESCA near-ambient pressure spectrometer at 3.3 mBar pressure using monochromatic Al $K_\alpha$ (1.487 keV) radiation. The sample was mounted as a 6 mm pressed pellet into the XPS and $^{48}$Ar gas was used for charge compensation purposes. The surface atomic ratios of the O 1s and C 1s peaks were calculated in the CasaXPS software using a Shirley type background. X-ray powder diffraction (XRD) patterns were obtained using a Bruker D8 diffractometer with a Ni-filtered Cu $K_\alpha$ source at 40 kV and 40 mA, employing a scanning rate of 0.03 $\theta s^{-1}$ in the 2$\theta$ range from 5° to 60°, further details are shown in Fig. S2. The mean particle size distribution by volume (D [3,4]) of the ultrasonically-dispersed hydrothermal carbon in water was measured by laser diffraction (Mastersizer 2000E, Malvern).

### 2.5. Transmission electron microscopy

FIB prepared lamellae were imaged using a FEI Titan Themis$^3$ TEM fitted with a 4K CMOS digital camera (Gatan Oneview) after the STXM analysis. The FEG was operated at 80 kV in order to reduce C knock-on damage to the sample during imaging. Images were processed in Gatan Microscopy Suite and the FIJI distribution of ImageJ [33]. An attempt to obtain electron energy loss spectroscopy in scanning transmission electron microscope (STEM-EELS) spectral maps was not successful due to electron probe induced alteration.

### 2.6. STXM

X-ray spectromicroscopy was carried out at the Diamond Light Source (UK) using beamline I08. STXM offers improved spectral resolution and a reduction (~500 times) in dose compared to STEM-EELS, this comes at the expense of poorer spatial resolution [24–26]. At I08, a SX700 type plane grating monochromator ($0.25 \leq E \geq 4.4$ KeV), using synchrotron radiation from the 1st to 5th harmonic of an APPLE-II type insertion device is used. A monochromatic, focussed X-ray microprobe was formed by a zone plate optic, and undesired diffraction was removed by an order-selecting aperture (Fig. 1).

2D optical density ($O.D. = -\ln(I_{trans}/I_0)$) images were produced by raster scanning an interferometrically controlled sample stage. STXM spectromicroscopy was used to produce a carbon-specific chemical map of the FIB-prepared lamellae. Image stacks (6 × 6 μm) were acquired with ~40 nm spatial resolution, 5 ms dwell time and 0.15 eV spectral resolution over the main features of the carbon *K* edge (283–300 eV), and 0.5 eV resolution in the energy regions below (280–283 eV) and above (300–320 eV) the carbon *K* edge region. As-received signals were converted to optical density using incident signal ($I_0$) measurements from an adjacent, empty region of the image above the carbon *K* edge (284.5 eV).

Post-experiment treatment of the STXM-NEXAFS data was initially performed using the Mantis spectromicroscopy software. Mantis was used to normalize the carbon *K* edge spectra, subtract dark current (typically ~90 counts) and correct for spatial drift in the image [34]. The Mantis software was also used to conduct a principal component (PCA) and cluster (CA) analysis, whereby a set of eigenimages and eigenspectra from the data covariance matrix are classified into clusters of pixels of similar spectral response. Further details on the workflow and analysis performed using Mantis may be found in the publication by *Lerotic* et al. [34]. Normalised, dark signal and drift corrected NEXAFS spectra from the core and shell of the hydrothermal carbon particle then underwent spectral deconvolution using the LARCH and LMFIT python packages [35,36]. Spectral deconvolution by non-linear least squares fitting was performed using five Gaussian functions with centroid energy positions set as those of key carbon functional groups taken from literature and reference samples (Table 1). The full width half maximum (FWHM) of these Gaussian functions were considered as a convolution of experimental energy resolution and physical peak broadening due to the chemistry of the material. The Gaussian FWHM were initially set at 0.2 eV, approximating the energy resolution of the instrument, then allowed to vary between 0.3 and 0.5 eV. In the fitting, the ionisation potential (IP) step was represented by an exponentially modified error function, as described by *Stohr* et al. [37].

## 3. Results and discussion

### 3.1. Elemental analysis and morphology

High resolution, secondary electron, SEM images of the produced glucose-derived hydrothermal carbons produced at 200 °C (HTC200) and 250 °C (HTC250) are shown in Fig. 2. In agreement with other studies, the spherules appear to increase in average diameter with process temperature, from ~500 nm at 200 °C to ~3 μm at 250 °C [11]. Particle growth was also observed using laser diffraction particle size analysis, where the volume-weighted mean diameters were found to be 7.51 μm and 12.83 μm for HTC200 and HTC250 respectively. The larger particle sizes observed using laser diffractometry are likely due to particle agglomeration, which is clearly observed by SEM imaging (Fig. 2). XRD collected for both HTC200 and HTC250 show a single broad peak, centred at 23° (Fig. S2), confirming an amorphous structure.

In order to investigate changes in oxygen to carbon ratios (O:C) between the surface and bulk of HTC250, surface-biased O:C were collected using XPS (~10 nm penetration depth) and compared to O:C from traditional bulk elemental analysis. Significant changes in O:C might indicate changes in carbon chemistry between the interface and bulk of hydrothermal carbon (Table 2). Bulk O:C ratios for HTC200 and HTC250 were found to be 0.28 ± 0.01 and 0.22 ± 0.01 respectively, and conform to other literature studies of glucose-derived hydrothermal carbon [10]. XPS, as previously discussed, was conducted at near-ambient pressure to reduce any loss of surface-carbon functional groups due to volatilisation. Fitting of the ambient pressure XPS data (Fig. S3) for HTC250 gave a surface O:C of 0.217, which is within standard error of the recorded bulk value from elemental analysis. Although the similar O:C ratios between the surface and the bulk of HTC250 suggest broad similarity in the overall abundance of O and C throughout the structure, it does not provide information regarding chemical speciation and bonding within HTC250. Carbon moieties at the surface could differ from the bulk of the material while maintaining similar O:C ratios.

### 3.2. Evidence for shell-core structure

Since bulk scale analyses showed no significant change in O:C between the surface and bulk of HTC250, nanometre-scale imaging (TEM and STXM) were conducted on a FIB-sectioned spherule of the same material. STXM analyses were found to be unsuitable for

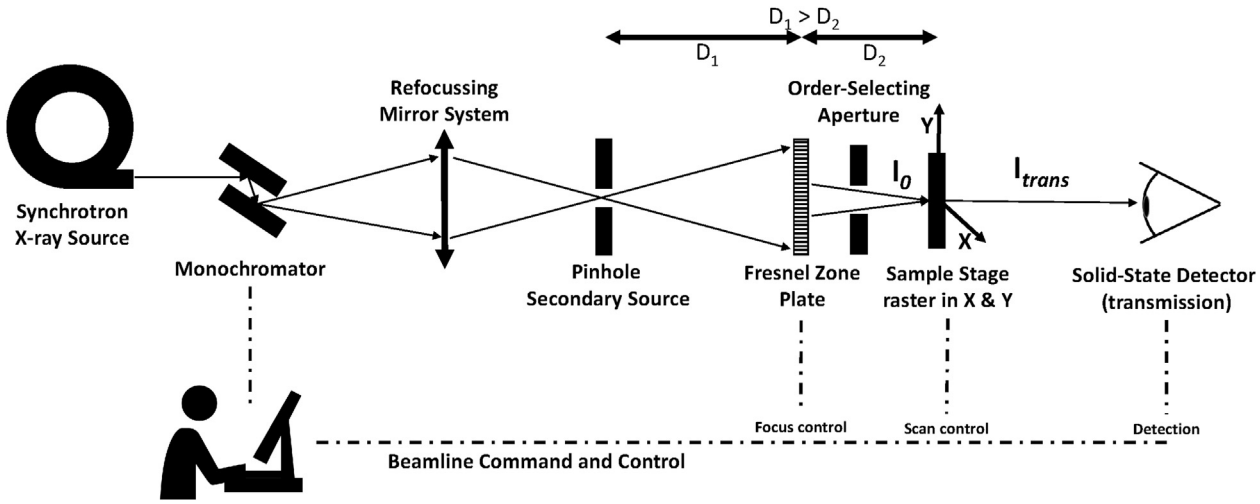


**Fig. 1.** Simplified diagram of the scanning transmission X-ray microscope in operation at I08. $I_0$: incident X-rays, $I_{trans}$: transmitted X-rays.

**Table 1**
Summary of Gaussian peak locations and functional group assignment for carbon *K*-edge NEXAFS spectra in this study.

| Transition Energy (eV) | Functional Interpretation | Transition | Reference |
|---|---|---|---|
| *284.8* | C=C aromatic [benzene-type building blocks] | 1s-π* | [21,38–41] |
| *285.3* | C=C-X Aryl-linked group [X = O, C] | 1s-π* | [41–43] |
| *286.6* | C=C–O furan | 1s-π* | [39,41,44,45] |
| *287.5* | aliphatic C–H | 1s-σ* | [44,46] |
| *288.2* | C=O–OH carboxyl group, C=O aldehyde group | 1s-π* | [21,41,44] |

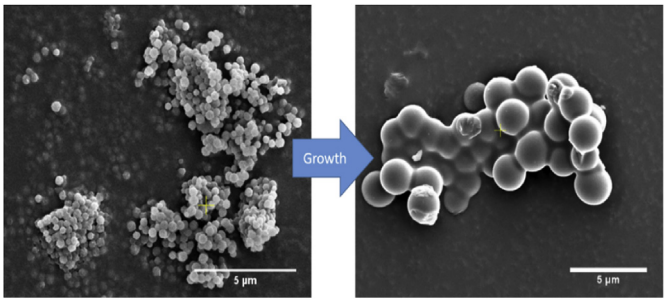


**Fig. 2.** FEG-SEM images. Glucose Hydrothermal Carbon produced at 200 °C (left) and 250 °C (right) from this study. The increase in size with process temperature is visible. (A colour version of this figure can be viewed online.)

HTC200 due to the smaller size of the produced spherules, making a representative spectral analysis infeasible, hence all further analysis was performed using HTC250. Fig. 3a and b show a false-colour, chemically sensitive STXM optical density micrograph and a high resolution TEM image of HTC250 respectively. Hydrothermal carbon has been hypothesised to form *via* the coalescence of smaller spheres [12,15,17]. The STXM images show no evidence of sub-domains of dissimilar carbon chemistry that could support a coalescence mechanism. However, growth by coalescence may not be ruled out by this observation alone, since coalesced spheres could potentially form a homogenous single spherule. A STXM image collected at an X-ray energy of 286.6 eV achieved the highest contrast between the surface and bulk of the HTC250 lamella and a clear shell-core type structure is observed (Fig. 3a). In the carbon *K* edge, 286.6 eV corresponds to the α carbon 1s-$\pi^*_{C=C-O=}$furan transition energy (Table 1) and for clarity, Fig. 3c shows the α-carbons (C1, C4) and β-carbons (C2, C3) in the HMF molecule. In the TEM image (Fig. 3b), the shell appears as darker in bright field, indicating an annulus of increased mass thickness around the particle. The presence of this region in both the STXM and TEM images indicate that the shell is not simply a thickness artefact in the STXM optical density map. The shell, in both STXM and TEM was measured to be 100–200 nm in width. The presence of physisorbed organic species (e.g. levulinic acid), have been shown to be present on the surface of hydrothermal carbon [47]. This identification of a shell-core type structure of differing carbon chemistry in hydrothermal carbon, as will be discussed, has significant implications for proposed growth mechanisms, and is unlikely to be simply due to physisorbed levulinic acid.

### 3.3. Investigation of shell and core functionality by spectral deconvolution

Observation of a core-shell type structure for HTC250 led to an investigation of changes in carbon speciation between the core and

**Table 2**
Yield and bulk elemental analysis of hydrothermal carbons. Errors propagated from triplicate results.

| Sample | Component (wt %) | | | | | Atomic Ratio | |
|---|---|---|---|---|---|---|---|
| | Yield | C | H | N | O | H:C x10 | O:C |
| HTC200 | 55.4 | 61 ± 2 | 4.1 ± 0.2 | 1.21 ± 0.07 | 17.0 ± 0.4 | 0.67 ± 0.04 | 0.28 ± 0.01 |
| HTC250 | 60.5 | 66.2 ± 0.7 | 4.0 ± 0.1 | 1.14 ± 0.04 | 14.6 ± 0.2 | 0.60 ± 0.02 | 0.22 ± 0.01 |

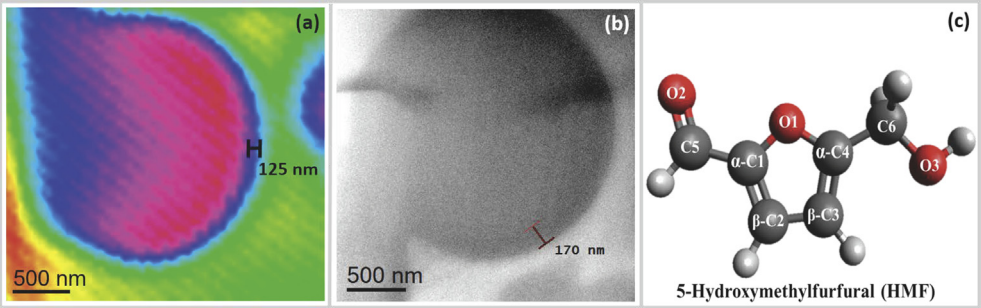


**Fig. 3.** FIB-sectioned HTC250 lamella imaged using (a) STXM (286.6 eV) and (b) TEM microscopy. Estimated shell thicknesses are super-imposed upon the images. (c) shows the 5-Hydroxymethylfurfural (HMF) molecule with the relevant α and β carbons highlighted. (A colour version of this figure can be viewed online.)

shell. In order to investigate these differences, PCA and CA were performed on the STXM stack. The number of significant components during the CA was taken as the inflection point of the PCA scree-plot (Fig. S4); the use of four components minimised the CA mean square error. The four components in the CA correspond to: (i) the platinum/thicker layer applied during FIB lift-out; (ii) the resin background; (iii) the shell region; and (iv) the core region (Fig. S5).

The resulting CA for the core-shell components can be seen in Fig. 4a. Pixels in blue represent the core region of the hydrothermal carbon lamella, and pink pixels represent the shell region. The clear shell-core components confirm the presence of chemical differences. NEXAFS spectra for the corresponding shell and core regions exhibit three main peaks at 285 eV, 287 eV and 288 eV (Fig. 4b). The relatively small spectral changes between core and shell are expected, since these changes occur across a single hydrothermal carbon sphere. Neither the core nor the shell NEXAFS spectra exhibit a 1s-$\pi^*_{COO}$ transition (~290.3 eV), indicating the absence of both carbonate and carbohydrate (e.g. glucose) species in the HTC250 lamella. The combination of (i) a lack of fine structure at the aromatic 1s-$\sigma^*_{C=C}$ transition (~293 eV) and (ii) the broad nature of the corresponding XRD pattern for HTC250 (S2) suggest that no ordered polyaromatic component is present in either the core or shell. Despite their similarity however, significant chemical differences between the shell and core of HTC250 are observed. Using known electron transitions (Table 1), we summarise these three differences as: (i) a broader C=C$_{arom}$ peak in the core spectrum (ii) a change in peak area ratios between the aromatic 1s-$\pi^*_{C=C}$ (~285.0 eV) and α-carbon furan 1s-$\pi^*_{C=C-O}$ (~286.6 eV) transitions and (iii) a broader aldehyde/carboxyl 1s-$\pi^*_{C-O}$ (~288.2 eV) shoulder in the shell spectrum. In order to quantify the observed changes, Gaussian spectral deconvolution was performed. Since neither the carbonate 1s-$\pi^*_{COO}$ (290.3 eV) nor aromatic 1s-$\sigma^*_{C=C}$ (292 eV) transitions were observed, these transition energies were not modelled. By decreasing the total number of independent fitting parameters, the accuracy of the model was improved in accordance with the Nyquist criterion [37]. The results of the spectral deconvolution of the core and shell spectra were achieved with reduced $\chi^2$ values of 0.029 and 0.021 respectively (Fig. 5). Resultant peak areas and FWHM are shown in Table 3. Three key changes moving from the core to shell spectra are observed and each of these is identified and discussed in the following sections.

### 3.3.1. – 285 eV: core condensation

The first of the three key changes observed in the core to shell spectra is broadening of the lowest energy feature at ~285 eV (Fig. 4b) which may be interpreted as two distinct, yet highly correlated carbon moieties: aromatic C=C groups (284.8 eV) and

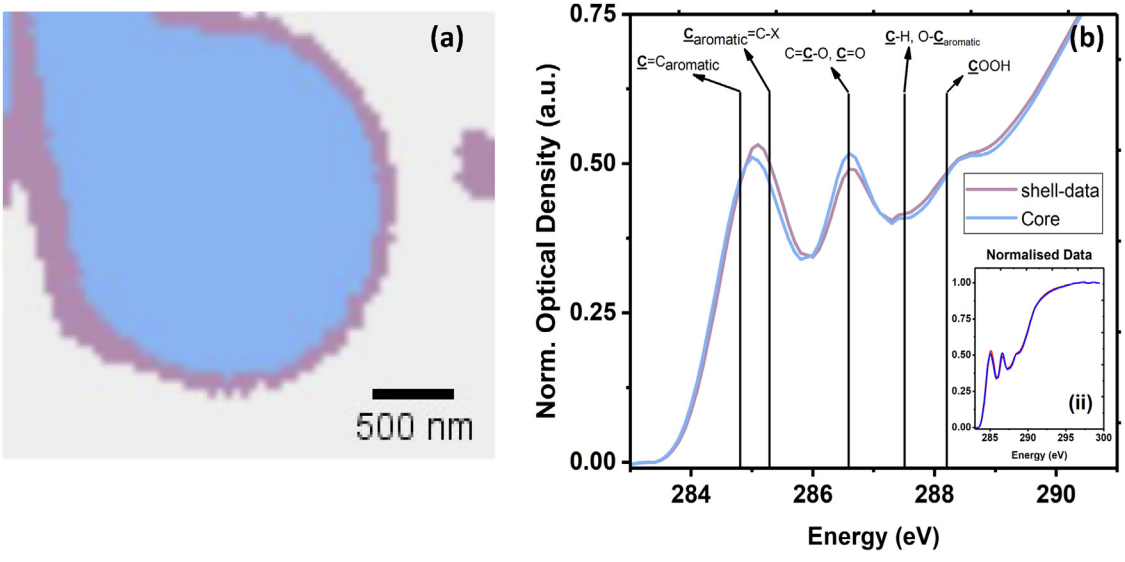


**Fig. 4.** Results of principle component and cluster analysis. (a) Cluster map of core (blue) and (shell) components. (b) NEXAFS spectra from the core (blue) and shell (pink) with carbon transitions (Table 1) labelled. Unit Normalisation is shown in b(ii). (A colour version of this figure can be viewed online.)

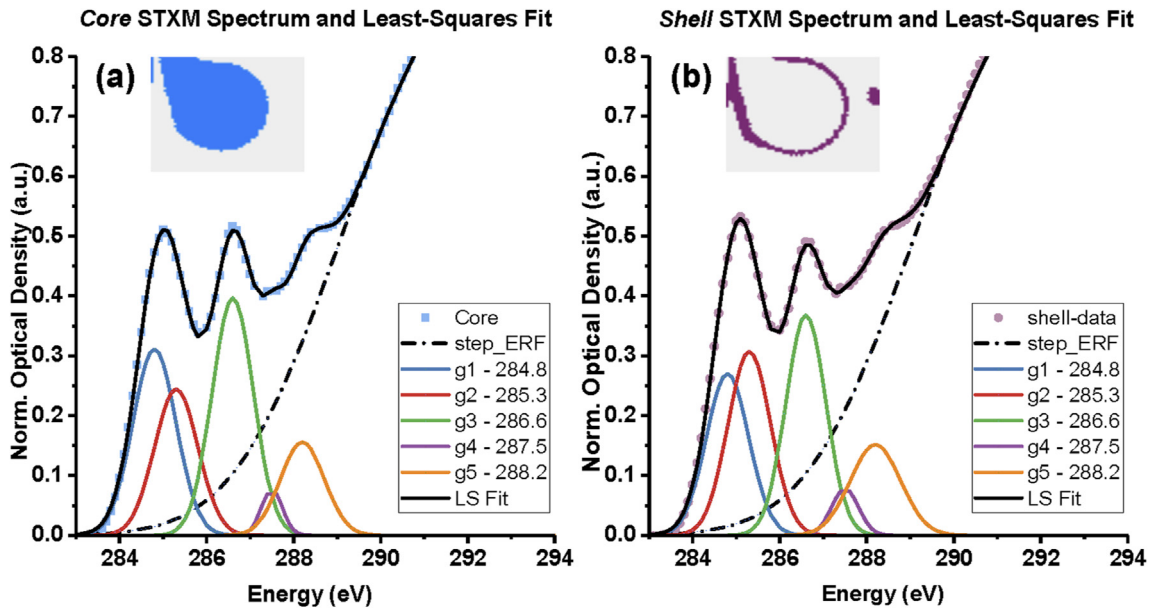


**Fig. 5.** STXM generated NEXAFS spectra with the five components of Gaussian deconvolution and the corresponding fit for both (a) the core and (b) the shell. Inset is the result of principal component analysis showing the regions used to generate the core and shell NEXAFS spectra. (A colour version of this figure can be viewed online.)

**Table 3**
Parameters for Gaussian spectral deconvolution of the principal components (core and shell) with standard errors.

| Transition | Gaussian Centroid Energy (eV) | Core | | Shell | |
|---|---|---|---|---|---|
| | | FWHM (eV) | Area (a.u.) | FWHM (eV) | Area (a.u.) |
| 1s-π* Aromatic; C=C | 284.8 | 1.17 ± 0.03 | 0.31 ± 0.01 | 1.15 ± 0.03 | 0.27 ± 0.01 |
| 1s-π* Aromatic-Aryl; C=C-X | 285.3 | 1.17 ± 0.03 | 0.24 ± 0.02 | 1.15 ± 0.03 | 0.31 ± 0.02 |
| 1s-π* Furan; C=C–O | 286.6 | 1.12 ± 0.05 | 0.40 ± 0.01 | 1.08 ± 0.05 | 0.36 ± 0.01 |
| 1s-σ* Aliphatic; C–CH | 287.5 | 0.57 ± 0.08 | 0.06 ± 0.02 | 0.73 ± 0.10 | 0.08 ± 0.01 |
| 1s-π* Carboxyl; C–OOH | 288.2 | 1.19 ± 0.08 | 0.16 ± 0.01 | 1.36 ± 0.07 | 0.15 ± 0.01 |
| 1s-π* Aldehyde; CH=O | | | | | |

heteroatomic-aryl C=C-X groups (285.3 eV). HTC250 is principally formed of C and O, and since C–O transitions are known to occur at higher energies, the latter heteroatomic-aryl moiety is assigned to aryl C=C–C groups. Interpreting the initial 285 eV peak as two overlapping functionalities is guided by previous experimental NEXAFS studies and dynamic functional theory (DFT) calculations [42,44,48]. During the first stages of hydrothermal carbon growth, polycondensation reactions are thought to occur between aqueous HMF molecules, forming three dimensional oligomers with a furanic local structure [16]. Nascent hydrothermal carbon is principally formed of furan rings interlinked by aryl units, either at the α (C-O) or β (C=C) carbon positions on the furan ring. During hydrothermal carbon formation, it is supposed that these linking units undergo condensation, forming a more aromatic bulk substructure [39,49]. In the spectral deconvolution, a 23% decrease in aryl 1s-$\pi^*_{C=C-C}$ (285.3 eV) transition peak area (Table 3) between the shell and core of HTC250 is observed. Limited area under the aryl peak in the core spectra highlights the loss of aryl functionality between the surface and bulk in HTC250. The lack of aryl functionality in the core supports the argument that aryl species are removed in condensation reactions during hydrothermal carbon formation [17]. The observed loss in aryl functionality from shell to core is concomitant with a 13% enhancement in aromatic C=C (284.8 eV) peak area (Table 3). Enhanced core aromaticity coupled with inhibited surface aryl functionality may be interpreted as initial surface formation, followed by a series of condensation reactions during growth. Moieties linked at the β carbon atom result in an increase in the peak amplitude at the 1s-$\pi^*_{C=C}$ transition. Therefore, condensation is likely occurring *via* shortening or removal of α carbon linkers concomitant with the formation of β carbon bonding. An increasing in the abundance of β linking units, and lower abundance of α units suggest formation of clusters of arene functionality and three membered furanic units [11,12,49].

### 3.3.2. – 285 eV to 287 eV: inhomogeneous distribution of furan species

The second of the three changes observed in the core to shell spectra is a change in peak ratio between the aromatic C=C (284.8 eV) and furan C=C–O (286.6 eV) peaks (Fig. 4b). The 286.6 eV peak has previously been assigned as the furan 1s-$\pi^*_{C=C-O}$ transition in soft X-ray NEXAFS of model hydrothermal carbons [38,39]. Although furan units are known to be present in both the surface and bulk of hydrothermal carbon, the distribution of furan units within a single spherule remains unknown. HMF is the principal monomer in hydrothermal carbon formation and it has previously been assumed that furan-type C=C–O carbon is uniformly distributed within hydrothermal carbon [15]. However, here the spectral deconvolution shows a 10% decrease in the amplitude of the furan C=C–O transition (286.6 eV) between the core and shell NEXAFS spectra (Fig. 5 and Table 3). The inhomogeneous distribution of furan moieties between shell and core is incongruous with a simple model of hydrothermal carbon growth by HMF polymerisation alone. Dehydration reactions are likely the principal pathway in the core of the hydrothermal carbon spherule.

Nonetheless, the lower abundance of furan functionality at the shell indicates an intermediate reaction pathway at the water-carbon interface.

### 3.4. - 288.2 eV: the water-carbon interface

The third of the three changes observed in the core to shell spectra is a change in peak broadening at the 1s-$\pi^*_{C-O}$ (aldehyde/carboxyl) transition in the 288 eV region (Fig. 4b). Previous literature suggests that intermediate pathways at the hydrothermal carbon surface may include aldol condensation reactions and acid-catalysed ring opening [12]. Such pathways lead to the production of reactive, dehydrated, carboxylic acid and aldehyde functionalities in HCW. Changes in aldehyde and carboxylic functionality are known to result in changes at the 1s-$\pi^*_{C-O}$ (aldehyde/carboxyl) transition in the 288 eV region. Our results show an increased FWHM at the 1s-$\pi^*_{C-O}$ (aldehyde/carboxyl) transition in the shell region (Table 3). The observed broadening of the 1s-$\pi^*_{C-O}$ transition suggests an increased distribution of aldehyde C–OH (287.5 eV) and carboxyl C–OOH functionalities at the hydrothermal carbon surface. Although caution must be exercised in attributing an increased distribution of aldehyde/carboxyl surface functionality to a single pathway, aldol condensation reactions are likely responsible for producing an increased distribution of aldehyde/carboxyl functionalities [5,50]. Furthermore, as previously discussed, physisorbed levulinic acid is likely present on the surface of hydrothermal carbon. A DFT calculation performed for levulinic acid (Fig. S6), indicates that any changes due to the presence of levulinic acid would occur primarily at the 1s-$\pi^*_{C-O}$ (aldehyde/carboxyl) transition. Therefore, it is likely that the observed broadening of this feature may be influenced by physisorbed organics. In either case, we suggest that an increased distribution of surface aldehyde/carboxyl functionality may provide a conducive environment for hydrothermal growth with aqueous monomers (e.g. HMF).

### 3.5. Comments on hydrothermal carbon growth and further work

The formation mechanism for hydrothermal carbon has been widely postulated. Evidence for such mechanisms has been impeded by a lack of direct spectroscopic techniques able to spatially resolve carbon functionality within hydrothermal carbon particles. Previous TEM and $^{13}C$ NMR studies have found that initial hydrothermal carbon growth is from oligomers formed of HMF in HCW. Phase separation of nascent hydrothermal carbon from the process water likely occurs by the formation of a hydrophobic core due to condensation of HMF. The STXM (and TEM) results presented here provide clear evidence for a core-shell model with different carbon chemical bonding environments for a glucose-derived hydrothermal carbon produced at 250 °C. NEXAFS spectroscopy here highlights a hydrothermal carbon core with increased aromatic and furanic functionality, presenting a more condensed, hydrophobic core. The shell displays a broader distribution of carboxylic and/or aldehyde functionality and is less aromatic. Using this information, a mechanism for hydrothermal carbon growth can be put forward. A schematic cartoon illustrating these findings is presented in Fig. 6.

The proposed growth mechanism of glucose derived hydrothermal carbon is by hydrophobic-ripening and this is supported by kinetic modelling in other studies [6]. In contrast to previously proposed hydrophobic ripening mechanisms, the evidence from STXM suggests that (i) a core-shell structure *is* present and (ii) growth does not occur *via* cleavage of the carboxyl terminal unit in HMF. Our results suggest that nucleation and growth can be described in four stages: Stage 1 – HMF is produced from the dehydration of glucose in HCW and acts as the key monomer for hydrothermal carbon growth. Stage 2 – We observe a carboxyl/aldehyde rich shell layer, likely produced by the acid-catalysed ring opening of local HMF monomers or through aldol condensation of local carboxylic acids, which may act as a binding site for local HMF. Stage 3 - As the hydrothermal carbon grows, the shell layer undergoes dehydration and condensation reactions (e.g. Diels-Alder reactions). Stage 4 - In the core, dehydration and condensation reactions appear to dominate which leads to the removal or shortening of HMF α-carbon aryl linking units as well as the formation of β-carbon links, increasing the aromatic spectral response. Linkages at the furan β-carbon position produce a more condensed and hydrophobic hydrothermal carbon core. In light of kinetic modelling studies indicating the growth of hydrothermal carbon in stages, it is possible that different chemical pathways are available during the stages of hydrothermal carbon growth. HTC250 was produced under relatively severe conditions (250 °C, 1 h) and might only represent the final stage of growth. Further STXM studies are required at different stages of HTC formation, especially for other model carbohydrates over a range of reaction temperatures. It is unfortunately not possible to completely rule out the effect of

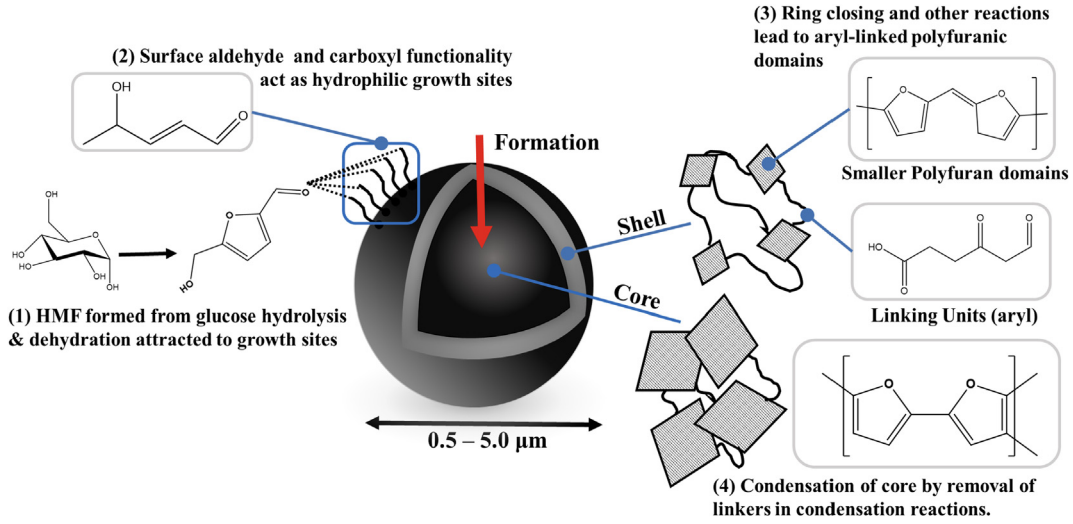


**Fig. 6.** Cartoon depiction of proposed formation mechanism from this study. (A colour version of this figure can be viewed online.)

physisorbed organics in the important feature at the 1s-$\pi^*_{C-O}$ transition, further work should be carried out to ascertain how such surface functionality behaves *in-situ*. Hydrothermal carbon formation is a complex chemical process necessitating *in-situ* work to support proposed mechanisms. Future studies testing the effects of inorganics, other lignocellulosic components and chemical additives are also vital in taking HTC forward as a viable biorefinery route to valorised, functional materials.

## 4. Conclusions

Spatially resolved X-ray spectromicroscopy has been applied to a model glucose-derived hydrothermal carbon. STXM provides the first direct, element-specific, spectroscopic evidence for a core-shell structure of glucose-derived hydrothermal carbon. A shell region with an approximate annular diameter of 100–200 nm was observed. Principal component and cluster analyses identified differential carbon chemistry between the shell and the core of the hydrothermal carbon spherule. Region-specific NEXAFS spectra for the core and shell support the assertion that hydrothermal carbon is principally formed of furan-type subunits interconnected by α-carbon *via* aryl-type linkers. No ordered aromatic component was found in either the shell or core of HTC250. Gaussian spectral deconvolution provides evidence for a core with increased furan subunit abundance and decreased aryl functionality, suggesting the condensation of aryl-linked furan subunits in the core. Deconvolution also demonstrates that the surface is enriched in an increased range of carboxyl and aldehyde functionalities. This evidence is used to suggest that different formation pathways are present between the core and shell. In the core, it is considered that growth is dominated by dehydration reactions, removing aryl linking units and forming β-linked furanic domains and arene clusters. At the surface, the observed increase in carboxyl and aldehyde functionalities points to other formation pathways enabled by the presence of aqueous 5-hydroxymethylfurfural in hot compressed water. We suggest that aldol condensation or catalysed ring opening may produce the observed surface carbonyl functionality.

## Credit author statement

Luke J.R. Higgins: Conceptualization, Methodology, Investigation, Writing - Original Draft, Writing - Review & Editing.

Andy P Brown: Investigation, Writing - Review & Editing, Supervision.

John P Harrington: Investigation, Writing - Review & Editing.

Andrew B Ross: Supervision, Resources.:

Burkhard Kaulich: Methodology, Investigation, Writing - Review & Editing.

Bhoopesh Mishra: Conceptualization, Methodology, Investigation, Writing - Review & Editing, Supervision.

## Declaration of competing interest

The authors declare that they have no known competing financial interests or personal relationships that could have appeared to influence the work reported in this paper.

## Acknowledgements

This work was supported by the Engineering and Physical Sciences Research Council [grant EP/L014912/1] as part of the UK Centre for Doctoral Training in Bioenergy at Leeds University. The authors would like to thank Diamond Light Source for beamtime (proposals SP19228 and MG22730), and the beamline staff Dr Tohru Araki and Dr. Majid Kazemian for their help and support during STXM experiments. Electron microscopy and focussed ion beam milling were carried out at the Leeds Electron Microscopy and Spectroscopy (LEMAS) centre. XPS data was collected by Dr. Elizabeth Willneff at the Versatile X-ray Spectroscopy Facility (VXSF). LEMAS and VXSF facilities are a part of the Bragg Centre at University of Leeds. Autors thank Dr. Elizabeth Wilneff for collecting XPS data and Dr. Jeanine Williams for collecting GC-MS data. LJRH thanks Mr Simon Lloyd and Dr Adrian Cunliffe for their suggestions, and Mr. Martin Fuller (Astbury Centre, University of Leeds) for his assistance in preparing ultra-microtomed lamellae.

## Appendix A. Supplementary data

Supplementary data to this article can be found online at https://doi.org/10.1016/j.carbon.2020.01.060.

## References

[1] F. Bergius, Beiträge zur Theorie der Kohleentstehung, Naturwissenschaften 16 (1928) 1–10, https://doi.org/10.1007/BF01504496.
[2] M.-M. Titirici, R.J. White, N. Brun, V.L. Budarin, D.S. Su, F. del Monte, J.H. Clark, M.J. MacLachlan, Sustainable carbon materials, Chem. Soc. Rev. 44 (2015) 250–290, https://doi.org/10.1039/C4CS00232F.
[3] M.-M. Titirici, R.J. White, C. Falco, M. Sevilla, Black perspectives for a green future: hydrothermal carbons for environment protection and energy storage, Energy Environ. Sci. 5 (2012) 6796–6822, https://doi.org/10.1039/c2ee21166a.
[4] M.-M. Titirici, A. Thomas, M. Antonietti, Back in the black: hydrothermal carbonization of plant material as an efficient chemical process to treat the CO2 problem? New J. Chem. 31 (2007) 787–789, https://doi.org/10.1039/b616045j.
[5] A. Kruse, E. Dinjus, Hot compressed water as reaction medium and reactant. Properties and synthesis reactions, J. Supercrit. Fluids 39 (3) (2007) 362–380, https://doi.org/10.1016/j.supflu.2006.03.016.
[6] D. Jung, M. Zimmermann, A. Kruse, Hydrothermal carbonization of fructose: growth mechanism and kinetic model, ACS Sustainable Chem. Eng. 6 (11) (2018) 13877–13887, https://doi.org/10.1021/acssuschemeng.8b02118.
[7] F.S. Asghari, H. Yoshida, Kinetics of the decomposition of fructose catalyzed by hydrochloric acid in subcritical water: formation of 5-hydroxymethylfurfural, levulinic, and formic acids, Ind. Eng. Chem. Res. 46 (23) (2007) 7703–7710, https://doi.org/10.1021/ie061673e.
[8] M.-M. Titirici, M. Antonietti, N. Baccile, Hydrothermal carbon from biomass: a comparison of the local structure from poly- to monosaccharides and pentoses/hexoses, Green Chem. 10 (2008) 1204–1212, https://doi.org/10.1039/b807009a.
[9] B.M. Kabyemela, T. Adschiri, R.M. Malaluan, K. Arai, Kinetics of glucose epimerization and decomposition in subcritical and supercritical water, Ind. Eng. Chem. Res. 36 (5) (1997) 1552–1558, https://doi.org/10.1021/ie960250h.
[10] M. Sevilla, A.B. Fuertes, The production of carbon materials by hydrothermal carbonization of cellulose, Carbon 47 (2009) 2281–2289, https://doi.org/10.1016/j.carbon.2009.04.026.
[11] C. Falco, N. Baccile, M.-M. Titirici, Morphological and structural differences between glucose, cellulose and lignocellulosic biomass derived hydrothermal carbons, Green Chem. 13 (2011) 3273–3281, https://doi.org/10.1039/c1gc15742f.
[12] S.K.R. Patil, C.R.F. Lund, Formation and growth of humins via aldol addition and condensation during acid-catalyzed conversion of 5-hydroxymethylfurfural, Energy Fuels 25 (10) (2011) 4745–4755, https://doi.org/10.1021/ef2010157.
[13] A.B. Fuertes, M. Sevilla, Chemical and Structural Properties of Carbonaceous Products Obtained by Hydrothermal Carbonization of Saccharides, Chem. Eur. J. 15 (2009) 4195–4203, https://doi.org/10.1002/chem.200802097.
[14] S.-A. Wohlgemuth, F. Vileda, M.-M. Titirici, M. Antonietti, A one-pot hydrothermal synthesis of tunable dual heteroatom-doped carbon microspheres, Green Chem. 14 (2012) 741–749, https://doi.org/10.1039/C2GC16415A.
[15] M. Zhang, H. Yang, Y. Liu, X. Sun, D. Zhang, D. Xue, Hydrophobic precipitation of carbonaceous spheres from fructose by a hydrothermal process, Carbon 50 (6) (2012) 2155–2161, https://doi.org/10.1016/j.carbon.2012.01.024.
[16] Y. Qi, M. Zhang, L. Qi, Y. Qi, Mechanism for the formation and growth of carbonaceous spheres from sucrose by hydrothermal carbonization, RSC Adv. 6 (2016) 20814–20823, https://doi.org/10.1039/c5ra26725k.
[17] M. Zhang, H. Yang, Y. Liu, X. Sun, D. Zhang, D. Xue, First identification of primary nanoparticles in the aggregation of HMF, Nanoscale Res. Lett. 7 (38) (2012) 1–5, https://doi.org/10.1186/1556-276X-7-38.
[18] C. Yao, Y. Shin, L.-Q. Wang, C.F. Windisch, W.D. Samuels, B.W. Arey, C. Wang, W.M. Risen, G.J. Exarhos, Hydrothermal dehydration of aqueous fructose solutions in a closed system, J. Phys. Chem. C 111 (42) (2007) 15141–15145, https://doi.org/10.1021/jp074188l.

[19] B. Watts, L. Thomsen, P.C. Dastoor, Methods in carbon K-edge NEXAFS: Experiment and analysis, J. Electron. Spectrosc. Relat. Phenom. 151 (2) (2006) 105–120, https://doi.org/10.1016/j.elspec.2005.11.006.
[20] J. Stöhr, Analysis of Condensed, Chemisorbed, and Polymeric Molecules: An Overview, NEXAFS Spectroscopy, 2nd, Springer, Heidelbeg, 1992.
[21] D. Solomon, J. Lehmann, J. Wang, J. Kinyangi, K. Heymann, Y. Lu, S. Wirick, C. Jacobsen, Micro- and nano-environments of C sequestration in soil: a multi-elemental STXM-NEXAFS assessment of black C and organomineral associations, Sci. Total Environ. 438 (2012) 372–388, https://doi.org/10.1016/j.scitotenv.2012.08.071.
[22] K. Heymann, J. Lehmann, D. Solomon, B. Liang, E. Neves, S. Wirick, Can functional group composition of alkaline isolates from black carbon-rich soils be identified on a sub-100nm scale? Geoderma 235–236 (2014) 163–169, https://doi.org/10.1016/j.geoderma.2014.07.011.
[23] M. Plaschke, J. Rothe, M. Altmaier, M.A. Denecke, T. Fanghänel, Near edge X-ray absorption fine structure (NEXAFS) of model compounds for the humic acid/actinide ion interaction, J. Electron. Spectrosc. Relat. Phenom. 148 (2005) 151–157, https://doi.org/10.1016/j.elspec.2005.05.001.
[24] A. Naber, M. Plaschke, J. Rothe, H. Hofmann, T. Fanghänel, Scanning transmission X-ray and laser scanning luminescence microscopy of the carboxyl group and Eu(III) distribution in humic acid aggregates, J. Electron. Spectrosc. Relat. Phenom. 153 (2006) 71–74, https://doi.org/10.1016/j.elspec.2006.06.005.
[25] A. Braun, A. Kubatova, S. Wirick, S.B. Mun, Radiation damage from EELS and NEXAFS in diesel soot and diesel soot extracts, J. Electron. Spectrosc. Relat. Phenom. 170 (1–3) (2009) 42–48, https://doi.org/10.1016/j.elspec.2007.08.002.
[26] A.P. Hitchcock, J. Li, S.R. Reijerkerk, P. Foley, H.D.H. Stöver, I. Shirley, X-ray absorption spectroscopy of polyureas and polyurethanes and their use in characterizing chemical gradients in thin-walled polyurea capsules, J. Electron. Spectrosc. Relat. Phenom. 156–158 (2007) 467–471, https://doi.org/10.1016/j.elspec.2006.11.061.
[27] B.A. Collins, H. Ade, Quantitative compositional analysis of organic thin films using transmission NEXAFS spectroscopy in an X-ray microscope, J. Electron. Spectrosc. Relat. Phenom. 185 (5–7) (2012) 119–128, https://doi.org/10.1016/j.elspec.2012.05.002.
[28] J. Li, A.P. Hitchcock, H.D.H. Stöver, I. Shirley, A New Approach to Studying Microcapsule Wall Growth Mechanisms, Macromolecules 42 (7) (2009) 2428–2432, https://doi.org/10.1021/ma802130n.
[29] D. Covelli, D. Hernández-Cruz, B.M. Haines, V. Munoz, O. Omotoso, R. Mikula, S. Urquhart, NEXAFS microscopy studies of the association of hydrocarbon thin films with fine clay particles, J. Electron. Spectrosc. Relat. Phenom. 173 (1) (2009) 1–6, https://doi.org/10.1016/j.elspec.2009.02.012.
[30] S. Bernard, K. Benzerara, O. Beyssac, G.E. Brown, L.G. Stamm, P. Duringer, Ultrastructural and chemical study of modern and fossil sporoderms by Scanning Transmission X-ray Microscopy (STXM), Rev. Palaeobot. Palynol. 156 (1–2) (2009) 248–261, https://doi.org/10.1016/J.REVPALBO.2008.09.002.
[31] N. Hagemann, S. Joseph, H.P. Schmidt, C.I. Kammann, J. Harter, T. Borch, R.B. Young, K. Varga, S. Taherymoosavi, K.W. Elliott, A. McKenna, M. Albu, C. Mayrhofer, M. Obst, P. Conte, A. Dieguez-Alonso, S. Orsetti, E. Subdiaga, S. Behrens, A. Kappler, Organic coating on biochar explains its nutrient retention and stimulation of soil fertility, Nat. Commun. 8 (2017) 1–11, https://doi.org/10.1038/s41467-017-01123-0.
[32] A.M. Smith, S. Singh, A.B. Ross, Fate of inorganic material during hydrothermal carbonisation of biomass: influence of feedstock on combustion behaviour of hydrochar, Fuel 169 (2016) 135–145, https://doi.org/10.1016/j.fuel.2015.12.006.
[33] J. Schindelin, I. Arganda-Carreras, E. Frise, V. Kaynig, M. Longair, T. Pietzsch, S. Preibisch, C. Rueden, S. Saalfeld, B. Schmid, J.-Y. Tinevez, D.J. White, V. Hartenstein, K. Eliceiri, P. Tomancak, A. Cardona, Fiji: an open-source platform for biological-image analysis, Nat. Methods 9 (2012) 676–682, https://doi.org/10.1038/nmeth.2019.
[34] M. Lerotic, R. Mak, S. Wirick, F. Meirer, C. Jacobsen, MANTiS: A program for the analysis of x-ray spectromicroscopy data, J. Synchrotron Rad. 21 (2014) 1206–1212, https://doi.org/10.1107/S1600577514013964.
[35] M. Newville, Larch: an analysis package for XAFS and related spectroscopies, J. Phys. Conf. Ser. 430 (2013), 012007, https://doi.org/10.1088/1742-6596/430/1/012007.
[36] M. Newville, T. Stensitzki, D.B. Allen, A. Ingargiola, LMFIT: Non-Linear Least-Squares Minimization and Curve-Fitting for Python, Zenodo, 2014, 10.5281/zenodo.598352.
[37] D.A. Outka, J. Stöhr, Curve fitting analysis of near-edge core excitation spectra of free, adsorbed, and polymeric molecules, J. Chem. Phys. 88 (1988) 3539–3554, https://doi.org/10.1063/1.453902.
[38] K.G. Latham, W.M. Dose, J.A. Allen, S.W. Donne, Nitrogen doped heat treated and activated hydrothermal carbon: NEXAFS examination of the carbon surface at different temperatures, Carbon 128 (2018) 179–190, https://doi.org/10.1016/j.carbon.2017.11.072.
[39] K.G. Latham, M.I. Simone, W.M. Dose, J.A. Allen, S.W. Donne, Synchrotron based NEXAFS study on nitrogen doped hydrothermal carbon: insights into surface functionalities and formation mechanisms, Carbon 114 (2017) 566–578, https://doi.org/10.1016/j.carbon.2016.12.057.
[40] G.D. Cody, R.E. Botto, H. Ade, S. Behal, M. Disko, S. Wirick, Inner-shell spectroscopy and imaging of a subbituminous coal: in-situ analysis of organic and inorganic microstructure using C(ls)-, Ca(2p)-, and Cl(2s)-NEXAFS, Energy & Fuels 9 (1995) 525–533, https://doi.org/10.1021/ef00051a018.
[41] D. Solomon, J. Lehmann, J. Kinyangi, B. Liang, K. Heymann, L. Dathe, K. Hanley, S. Wirick, C. Jacobsen, Carbon (1s) NEXAFS spectroscopy of biogeochemically relevant reference organic compounds, Soil Sci. Soc. Am. J. 73 (2009) 1817–1830, https://doi.org/10.2136/sssaj2008.0228.
[42] C.-C. Tsai, J.-L. Chen, W.-P. Hu, Y.-S. Lin, H.-R. Lin, T.-Y. Lee, Y.T. Lee, C.-K. Ni, C.-L. Liu, Selectivity of peptide bond dissociation on excitation of a core electron: effects of a phenyl group, Chem. Phys. Lett. 660 (2016) 60–68, https://doi.org/10.1016/J.CPLETT.2016.07.064.
[43] J. Lehmann, B. Liang, D. Solomon, M. Lerotic, F. Luizão, J. Kinyangi, T. Schäfer, S. Wirick, C. Jacobsen, Near-edge X-ray absorption fine structure (NEXAFS) spectroscopy for mapping nano-scale distribution of organic carbon forms in soil: application to black carbon particles, Glob. Biogeochem. Cycles 19 (2005) 1–12, https://doi.org/10.1029/2004GB002435.
[44] K. Heymann, J. Lehmann Johannes, D. Solomon, M.W.I. Schmidt, T. Regier, C 1s K-edge near edge X-ray absorption fine structure (NEXAFS) spectroscopy for characterizing functional group chemistry of black carbon, Org. Geochem. 42 (2011) 1055–1064, https://doi.org/10.1016/j.orggeochem.2011.06.021.
[45] D. Solomon, J. Lehmann, J. Harden, J. Wang, J. Kinyangi, K. Heymann, C. Karunakaran, Y. Lu, S. Wirick, C. Jacobsen, Micro- and nano-environments of carbon sequestration: multi-element STXM-NEXAFS spectromicroscopy assessment of microbial carbon and mineral associations, Chem. Geol. 329 (2012) 53–73, https://doi.org/10.1016/j.chemgeo.2012.02.002.
[46] A.C. Scheinost, R. Kretzschmar, I. Christl, C. Jacobsen, Carbon group chemistry of humic and fulvic acid: a comparison of C-1s NEXAFS and 13C-NMR spectroscopies, in: 5th Humic Substances Seminar, Royal Society of Chemistry, Cambridge, 2001, pp. 39–48.
[47] L. Yu, C. Falco, J. Weber, R.J. White, J.Y. Howe, M.-M. Titirici, Carbohydrate-derived hydrothermal carbons: a thorough characterization study, Langmuir 28 (2012) 12373–12383, https://doi.org/10.1021/la3024277.
[48] B. Singh, Y. Fang, B.C.C. Cowie, L. Thomsen, NEXAFS and XPS characterisation of carbon functional groups of fresh and aged biochars, Org. Geochem. 77 (2014) 1–10, https://doi.org/10.1016/j.orggeochem.2014.09.006.
[49] C. Falco, F.P. Caballero, F. Babonneau, C. Gervais, G. Laurent, M.-M. Titirici, N. Baccile, Hydrothermal carbon from biomass: structural differences between hydrothermal and pyrolyzed carbons via13C solid state NMR, Langmuir 27 (23) (2011) 14460–14471, https://doi.org/10.1021/la202361p.
[50] X. Liang, B.S. Haynes, A. Montoya, Acid-Catalyzed ring opening of furan in aqueous solution, Energy Fuels 32 (4) (2018) 4139–4148, https://doi.org/10.1021/acs.energyfuels.7b03239.